LANGMUIR Article
Cite This: Langmuir 2019, 35, 2303−2312
pubs.acs.org/Langmuir

Surfactant-Free Process for the Fabrication of Polyimide Aerogel Microparticles

Nicholas Teo and Sadhan C. Jana*

Department of Polymer Engineering, The University of Akron, 250 South Forge Street, Akron, Ohio 44325-0301, United States

Supporting Information

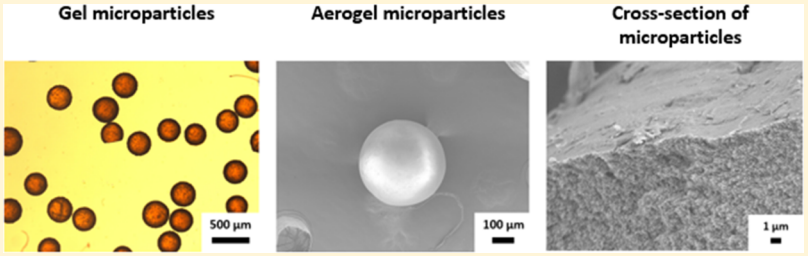

ABSTRACT: This work focuses on the fabrication of polyimide aerogel microparticles of diameter 200−1000 μm from a surfactant-free, two-phase, silicone oil/dimethylformamide (DMF) oil-in-oil (O/O) system using a simple microfluidic device. The polyimide sol prepared in DMF is turned into droplets suspended in silicone oil in the microfluidic device. The droplets are guided to a heated silicone oil bath to accelerate sol−gel transition and imidization reactions, thereby yielding spherical, discrete gel microparticles that do not undergo coalescence. The discrete gel microparticles are isolated and supercritically dried to obtain aerogel microparticles. The microparticle size distribution shows dependence on dispersed and continuous phase flowrates in the microfluidic channels. The microparticle surface morphology shows dependence on the silicone oil bath temperature.

INTRODUCTION

Aerogels are known for high porosities (often exceeding 90%) and high surface areas, reaching values up to 1000 m^2/g. Aerogel materials have been produced in several shapes such as monoliths,[1] microparticles,[2] and films and sheets.[3] Among these structural forms, cylindrical monoliths are most commonly studied because of their ease of fabrication. Kistler first reported silica aerogel monoliths in 1931.[4] Aerogels of several other precursor materials were later reported, such as syndiotactic polystyrene (sPS),[5,6] polyurea,[7−9] and polyimide.[10−12] In the past work, a large majority of aerogel articles were fabricated in monolithic forms and only a handful of studies reported flexible aerogel films.[3] Recently, monoliths of aerogel foams were reported with large fractions of macrovoids of typical diameter 30 μm, introduced in the structures of inherently meso- (pore diameter 2−50 nm) and macroporous (pore diameter > 50 nm) aerogels.[13−16] Gu and Jana[9] synthesized aerogel foams by filling the pores of a sacrificial bi-continuous polymer blend with polyurea sol−gel precursor materials. Teo and Jana[15] used water-in-oil (W/O) emulsion-templating method for the introduction of macrovoids in sPS aerogel monoliths. The emulsion-templating method was extended by Teo et al.[16] to oil-in-oil (O/O) emulsions to include macrovoid formation in mesoporous monolithic aerogels of moisture-sensitive monomers, such as the dianhydrides used in the synthesis of polyimide aerogels. The present work investigated a surfactant-free microfluidic process to obtain spherical, mesoporous polyimide aerogel microparticles of diameter 200−1000 μm.

Aerogel microparticles of diameter 50−200 μm may be advantageous in applications involving ion transport or ion adsorption, removal of noxious liquids, or delivery of drugs where large surface areas and short diffusion paths may be beneficial. Aerogel microparticles are of particular interest because of their ease of fabrication, ease of handling, and surface smoothness that prevent inflammatory responses from the body.[17] Aerogel microparticles derived from several bio-based polysaccharide materials such as chitin, chitosan, alginate, agar, cellulose, and starch have been reported.[18,19]

Typically, aerogel microparticles are produced via emulsion polymerization of precursor sol droplets stabilized by surfactants in an immiscible continuous liquid medium. The sol droplets originate from Rayleigh instability followed by stream breakup induced by mechanical mixing of a two-phase system.[20] In this method, the microparticle size distribution shows dependence on mixing speed, surfactant concentration, and the dispersed phase content. Because of the wide distribution of shear rate in mechanical mixing and undesired particle agglomeration by coalescence, a wide distribution of particle sizes is typically obtained. In preparing aerogel microparticles, another concern is attaining appropriate

Received: November 14, 2018
Revised: January 8, 2019
Published: January 16, 2019

DOI: 10.1021/acs.langmuir.8b03841
Langmuir 2019, 35, 2303−2312

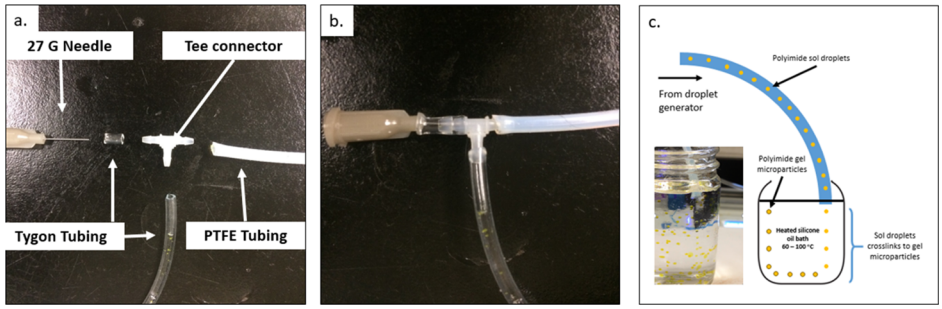

Figure 1. Droplet generator components (a) before and (b) after assembly. (c) Schematic of transfer of polyimide sol droplets into a heated silicone oil bath. The inset in (c) presents an image from experiments showing gel microparticles floating in the heated silicone oil bath.

emulsion stability, particularly for systems that need longer times for gelation.

A majority of emulsion polymerization processes utilize either an oil-in-water (O/W) or W/O system, for example, in the synthesis of silica microparticles.[21] However, O/W or W/O systems are not suitable for the fabrication of aerogel microparticles of moisture-sensitive monomer systems such as polyimides or for systems with appreciable solubility between the water and oil phases. Gu et al.[2] successfully adopted an O/O emulsion system to synthesize polyimide aerogel microparticles using a Span 85/Hypermer 1599 surfactant pairing. This system resulted in a broad particle size distribution, in the range 10−90 μm. Other surfactant-free and nonmechanical fabrication methods for aerogel microparticles have also been reported.[22] For example, Moner-Girona et al.[23] injected the silica sol directly into supercritical liquids such as acetone and carbon dioxide, whereas Zhang et al.[24] used an ambient pressure drying process based on injection of ammonia gas into a condensed silica solution dissolved in heptane.

One avenue to achieve greater control over particle size and particle size distribution is to capitalize on the accurate metering of microfluidic droplet generators. Droplet generation using microfluidic devices takes place in 5 different regimes, such as squeezing, dripping,[25] jetting,[26] tip-streaming, and tip-multibreaking.[27] Most microfluidic systems utilize viscous shear forces to form droplets and are built on a variety of device geometries such as cross-flow, co-flow, and flow-focusing to obtain the desired shear force fields.[28] In coflow geometry, the dispersed and continuous phase flows occur in parallel streams. The two-dimensional (2D) coflow geometry is configured using soft lithography,[29−33] whereas three-dimensional coflow devices are typically fabricated through spatial arrangements of the glass capillaries.[34,35]

To the best of our knowledge, a large majority of microfluidic droplet generation systems use either an O/W or W/O emulsion systems that are stabilized by the surfactants.[36] The O/O emulsion systems are inherently unstable owing to weak association of surfactants and appreciable mutual solubility of the two oil phases,[37] even though droplets can be more easily formed in O/O emulsion systems using microfluidic droplet generators. Also, the rates of droplet coalescence and Ostwald ripening are higher in O/O emulsions compared to W/O emulsion systems, resulting in rapid phase separation and formation of bilayer structures in O/O emulsions.[38] Thus, rapid coalescence observed for O/O emulsions even at high surfactant loading levels is a deterrent to obtaining substantial amounts of gel microparticles. This limitation is particularly important for the present study on polyimide gel microparticles as the timescale of the sol−gel transition in a polyimide system is typically longer than the timescale of stability of an O/O emulsion system. One may resort to using higher surfactant loadings to achieve greater stability in O/O emulsions, but the final aerogel microparticles may also retain greater proportions of surfactants.

This work seeks to circumvent the challenges in aerogel microparticle synthesis presented above, such as large particle sizes and wide particle size distributions, unstable O/O emulsion systems leading to significant coalescence, and the need for high surfactant concentration to attain acceptable emulsion stability. The objective was also to use a cheap and easily accessible continuous method to produce aerogel microparticles. To the best of our knowledge, this work is the first on the use of microfluidic flow setup for the fabrication of aerogel microparticles. Another key advantage of this work is the absence of surfactants, which in turn ensures cleanliness of the particles thus obviating the need for additional washing steps to remove undesired surfactant molecules as in surfactant-stabilized emulsions.

EXPERIMENTAL SECTION

Materials. Pyromellitic dianhydride (PMDA) was purchased from Alfa-Aesar (Haverhill, MA), and 2,2′-dimethylbenzidine (DMBZ) was purchased from Shanghai Worldyang Chemical Co., Ltd. (Shanghai, China). Tris(2-aminoethyl)amine (TREN) cross-linker was purchased from Sigma-Aldrich (Milwaukee, WI). Pyridine, acetic anhydride, acetone, and silicone oil were purchased from Fisher Scientific (Ontario, NY). *N*,*N*-Dimethylformamide (DMF) was purchased from VWR International (Radnor, PA). The components of the droplet generator, such as 27 G syringe, 0.16 cm inner diameter (ID) Tee connector, and Tygon tubing, were obtained from McMaster-Carr (Aurora, OH).

Fabrication of Droplet Generator. The coflow droplet generator used in this work was adapted from the work of Li et al.[39] This coflow droplet generator was assembled by inserting a 27 G flat tip needle with an ID of 0.2 mm into a 1.6 mm ID Tee connector. These two components were secured using a 1.6 mm ID Tygon tubing (Figure 1a). The assembled microfluidic coflow generator is shown in Figure 1b.

In this work, the dispersed and continuous phases were, respectively, polyimide sol in DMF with room temperature viscosity ∼1.98 mPa s and silicone oil with room temperature viscosity ∼48.6 mPa s. The interfacial tension between these two liquids at room temperature was measured to be 3.0 mN/m. For droplet generation, the dispersed phase flow rate was varied in the range 0.1−0.4 mL/min, which translated into a dispersed phase capillary number (Ca_d) of 0.015−0.059. The dispersed phase capillary number Ca_d is defined as the ratio of viscous and interfacial forces as shown in eq 1.

$$Ca_d = \frac{\mu v}{\sigma} \quad (1)$$

DOI: 10.1021/acs.langmuir.8b03841
Langmuir 2019, 35, 2303−2312

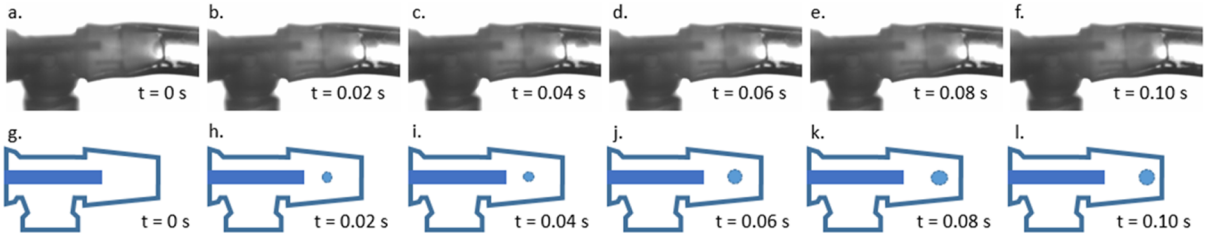

Figure 2. (a–f) Droplet generation in the jetting regime. The above sequence of images was captured using a high-speed camera at 1000 frames per second. Dispersed phase flowrate (Q_d) = 0.1 mL/min and continuous phase flowrate (Q_c) = 2 mL/min. (g–l) Corresponding schematic of droplet location in relation to the syringe tip.

In eq 1, μ is the dynamic viscosity, v is the velocity of the dispersed phase, and σ is the interfacial tension between the continuous and dispersed phases. The Weber number (We_d) of the dispersed phase calculated from eq 2 fell in the range of 0.15–2.34.

$$We_d = \frac{\rho v^2 l}{\sigma} \tag{2}$$

In eq 2, ρ is the density of the dispersed phase and l is the characteristic length. The continuous phase flow rate was varied between 2 and 8 mL/min, translating into continuous phase capillary numbers, Ca_c, of 0.29 and 1.17, respectively, for the above two flow rates using eq 1. The operating domain bounded by the above flow rates placed the droplet formation regime in this study within the jetting regime, as $Ca_c + We_d \geq O(1)$.[25,27,40] The jetting mechanism is clearly seen in the sequence of images captured using a high-speed camera, as presented in Figure 2. The images in Figure 2a–f indicate that droplets formed downstream from the internal syringe tip, thus establishing the jetting mechanism. Note, however, that the lighting condition did not allow imaging of the thin jet. The corresponding droplet locations inferred from the enlarged images in Figure 2a–f are schematically presented in Figure 2g–l to guide the eye. The flowrates of dispersed and continuous phase liquids used to capture the experimental images in Figure 2 represent the lowest values of Ca_c and Ca_d in the paper. This indicates that the jetting regime was also prevalent at higher flow rates, that is, higher Ca. The corresponding image capture of droplet generation at varying flowrates is included in the Supporting Information, Figure S1.

The jetting regime was chosen because of a number of considerations. First, the objective was to obtain the smallest possible droplet size for this setup. This made the jetting regime ideal, as at high Ca_c, the droplet size approaches the diameter of the dispersed phase delivery mechanism. Second, considering that the sol–gel transition time was relatively long (~26 min) and that sol–gel transition process was decoupled from the droplet generation process in this work, high rates of droplet generation also required high flowrates in the microfluidic flow system. Third, the dispersed phase flowrate was maintained above a minimum to generate droplets in highly viscous continuous phase silicone oil. This in conjunction with low interfacial tension values resulted in large values of Ca_d and placed the flows in the jetting regime. Fourth, as surfactants were not used in this work, special measures were taken to ensure that coalescence of droplets did not occur prematurely, for example, by droplet–droplet contacts within the microfluidic flow setup. The latter point required high continuous phase velocity to produce sufficient spacing between adjacent droplets. As a consequence, high Ca_c values were used, thus placing the flows in the jetting regime.

Preparation of Dispersed Phase Solution. The dispersed phase polyimide precursor solutions (henceforth sol) were prepared at room temperature by mixing PMDA, DMBZ, and TREN in DMF, as per the process outlined by Teo and Jana.[41] Briefly, PMDA and DMBZ, dissolved separately in DMF, were mixed with a magnetic stirrer at 1000 rpm for 2 min. Subsequently, TREN, acetic anhydride, and pyridine were added to trigger cross-linking reactions and to allow for the chemical imidization of the polyamic acid. The solution was magnetically stirred for an additional 1.5 min. A typical polyimide sol sample with 5.6 wt % polymer concentration was prepared using 0.160 g of PMDA, 0.159 g of DMBZ, 0.015 g of TREN, 0.50 g of acetic anhydride, 0.47 g of pyridine, and 5.0 mL of DMF. A higher than stoichiometric amount of TREN cross-linker was used to obtain appropriate gelation times.[41] After stirring, the polyimide sol was immediately transferred into a syringe pump for injection into the droplet generator.

Fabrication of Polyimide Aerogel Microparticles. The dispersed phase (polyimide sol) was injected at the specified flow rates through the 27 G needle (Figure 1a), whereas the continuous phase (silicone oil) was injected into the Tee connector through the Tygon tubing (Figure 1a). Both phases were delivered through Chemyx syringe pumps (Stafford, TX) at varying flowrates, for example, 0.1–0.4 mL/min for the dispersed phase and 2–8 mL/min for the continuous phase. The generated droplets were guided into a heated silicone oil bath for gelation and subsequent collection, as shown schematically in Figure 1c. Actual images of gel droplets floating in silicone oil are presented in the inset of Figure 1c.

The silicone oil bath was heated to 80 °C to enable fast gelation of the polyimide sol droplets. The quick gelation (in less than 10 s) of polyimide sol at this condition prevented coalescence of the droplets, thereby forming discrete, spherical polyimide gel microparticles. The gel microparticles were aged further in silicone oil for 24 h, removed from silicone oil, and washed with chloroform. The gel microparticles were subsequently solvent-exchanged sequentially with solvent mixtures consisting of 25 vol % acetone/75 vol % DMF, 50 vol % acetone/50 vol % DMF, 75 vol % acetone/25 vol % DMF, and finally with 100 vol % acetone each at 12 h intervals. In addition, the gels were further washed with 100 vol % acetone for an additional five times at 12 h intervals to remove as much of the DMF, silicone oil, and chloroform from the gels as possible. The gels were subsequently solvent-exchanged with liquid carbon dioxide in an autoclave by washing with 100 vol % liquid carbon dioxide six times at 1.5 h intervals. The liquid carbon dioxide filled gels were subsequently dried under supercritical condition of carbon dioxide at 50 °C and 11 MPa pressure to yield aerogel microparticles.

Characterization of Aerogel Microparticles. *Interfacial Tension Measurements.* The interfacial tension between the dispersed (DMF) and continuous (silicone oil) liquid phases was measured using a DuNouy tensiometer (Interfacial Tensiometer 70545, Central Scientific Co., VA) with data taken in triplicate.

Gel Time. The gel time of polyimide solution at room temperature (19–20 °C) was obtained from the crossover point of the storage and loss moduli of the sol measured using an ARES G2 Rheometer (TA Instruments, New Castle, DE). This also allowed for the collection of complex viscosity data. The polyimide sol was poured into a solvent trap and loaded into the rheometer fitted with a 50 mm cone. The rheometer was operated at a constant angular frequency of 1 rad/s and at 10% strain.

Gel and Aerogel Microparticle Size Distribution. The size distributions of gel and aerogel microparticles were studied using an Olympus BX51 optical microscope (OM). The images of a population of particles were collected and analyzed using the ImageJ software. Typically, the sizes of more than 100 particles were considered in each case.

Aerogel Morphology. The morphology of aerogels was studied using a scanning electron microscope (SEM, JSM5310, JEOL, MA) at

DOI: 10.1021/acs.langmuir.8b03841
Langmuir 2019, 35, 2303–2312

an accelerating voltage of 5 kV and emission current of 20 mA. A representative piece of fractured aerogel specimen was mounted on an aluminum stub using a carbon tape, followed by sputter coating with silver (ISI-5400 Sputter Coater, Polaron, UK).

Infrared. Infrared (IR) spectra were collected on a Nicolet iS50 FTIR tri-detector spectrophotometer (Thermo Scientific, MA).

Thermogravimetric Analysis. Thermogravimetric analysis (TGA) was conducted under N_2 with a Q50 thermogravimetric analyzer (TA Instruments, DE) using a heating rate of 20 °C/min, up to 700 °C.

Porosity and Pore Volume. Porosity was calculated from the values of skeletal (ρ_s) and bulk density (ρ_b), as shown in eq 3. The values of skeletal density were obtained using a helium pycnometer (AccuPyc II 1340, Micromeritics Instrument Corp., GA). Bulk density was obtained from the mass and volume of the aerogel specimens.

$$\text{Porosity} = \left(1 - \frac{\rho_b}{\rho_s}\right) \times 100\% \tag{3}$$

Total pore volume (V_{tot}) was calculated from the values of bulk and skeletal density, according to eq 4

$$V_{tot} = \frac{1}{\rho_b} - \frac{1}{\rho_s} \tag{4}$$

Note that only the bulk density of aerogel monoliths was obtained. The bulk density of aerogel microparticles could not be determined because of difficulty in isolating single particles for measurement of their diameter and weight.

Diameter Shrinkage. Bulk monolithic polyimide gels were synthesized in the cylindrical form in a mold of 13 mm in diameter and 26 mm in length. Diameter shrinkage of supercritically dried aerogel specimens was obtained from the diameter of the final dried aerogel and the diameter of the gel. For microparticles, the apparent diameter shrinkage was calculated from the average diameter of the gel and aerogel particles.

BET Surface Area. Brunauer–Emmett–Teller (BET) surface areas of aerogel specimens were obtained from N_2 adsorption–desorption isotherms at 77 K, using a Micromeritics Tristar II 3020 analyzer (Micromeritics Instrument Corp., GA). For monolithic aerogels, the pore volume of macropores ($V_{macropores}$) was deduced from total pore volume, V_{tot} and the volumes of mesopores ($V_{mesopores}$) and micropores ($V_{micropores}$). For this purpose, CO_2 adsorption–desorption isotherms at 273 K were obtained and combined with the N_2 isotherms using the nonlocal density functional theory model. The fraction of macropores, mesopores, and micropores were subsequently calculated according to eq 5.

$$\varphi_{macropores} = \frac{V_{macropores}}{V_{tot}};\ \varphi_{mesopores} = \frac{V_{mesopores}}{V_{tot}};\ \varphi_{micropores} = \frac{V_{micropores}}{V_{tot}} \tag{5}$$

RESULTS AND DISCUSSION

Properties of Aerogel Monoliths. We first characterized the aerogel monoliths as benchmark materials. The aerogel monoliths were synthesized following the same recipe of polyimide sol as was used in the synthesis of gel microparticles. The gel was cast in 13 mm cylindrical polypropylene molds at room temperature and supercritically dried after several steps of solvent exchange as described in the Experimental Section.

The polyimide aerogel monoliths exhibited a diameter shrinkage of 10.8%, skeletal density of 1.31 ± 0.01 g/cm^3, and bulk density of 0.053 ± 0.004 g/cm^3. These properties yielded a porosity of 96.0 ± 0.3% using eq 3 and pore volume of 18.2 ± 1.5 cm^3/g using eq 4.

Time Window for Droplet Generation. The gel time inferred from the crossover of the storage (G') and loss moduli (G'') of polyimide aerogel monoliths at room temperature was found to be 1570 s (~26 min), as shown in Figure 3. The gel

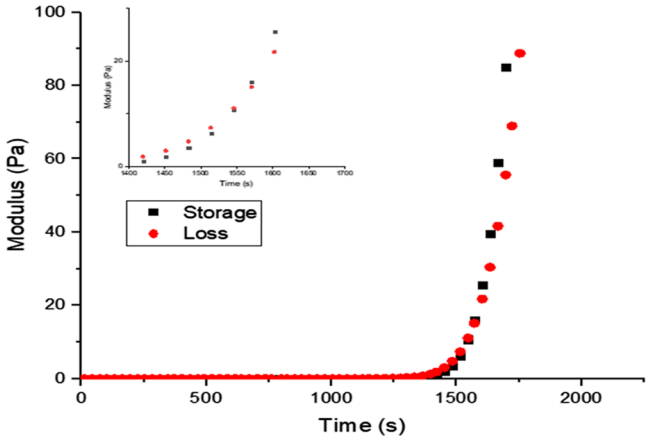

Figure 3. Evolution of storage (G') and loss moduli (G'') of polyimide sol at room temperature. The inset shows the crossover point at 1570 s (~26 min).

time provided a time window for droplet generation from the sol without clogging the droplet generator. In this work, droplets were generated within 5 min of preparation of the sol. The viscosity of the sol remained relatively constant over a 5 min period, varying from 1.98 mPa s right after sol preparation to 2.03 mPa s after 5 min. This guaranteed constant value of viscosity ratio of the continuous and dispersed phases during droplet generation. The generated droplets were conveyed into a bath of hot silicone oil as depicted schematically in Figure 1c. In the process, the sol droplets turned into gel microparticles because of faster cross-linking and chemical imidization reactions promoted by the hot silicone oil. An estimated gel time, as inferred from the time for the droplet to descend to the bottom of the silicone oil bath, was ~10 s. At the bottom of the oil bath, the particles remained discrete and did not coalesce, indicating that they had turned into cross-linked gel microparticles. Recall that the temperature of silicone oil bath was 80 °C.

Morphology of Gel and Aerogel Microparticles. The process described in the Experimental Section allowed successful formation of discrete aerogel microparticles. The OM and SEM images of representative gel and aerogel microparticles are presented in Figure 4. Both gel (Figure 4a) and aerogel microparticles (Figure 4b) were discrete and of spherical shapes. The SEM image in Figure 4c of a single aerogel microparticle shows a smooth surface and almost perfect spherical shape.

A set of representative SEM images in Figure 5 of fractured aerogel microparticles reveals the following trends. First, the aerogel microparticles had highly porous internal structures as evident from the images in Figure 5b,d. Second, the aerogel microparticles contained distinct skin morphology (Figure 5a,c), much denser than the internal structures. Third, a comparison of the microparticle skin layer in Figure 5c with that of monolith skin layer in Figure 5e reveals that aerogel monoliths had much more open pore structures in their skin layers than in the case of aerogel microparticles. Fourth, one can envision the skin layers of both the monolith and microparticles as 2D organizations of polyimide strands. Fifth, the monolith skin layers had thicker polyimide strands

DOI: 10.1021/acs.langmuir.8b03841
Langmuir 2019, 35, 2303–2312

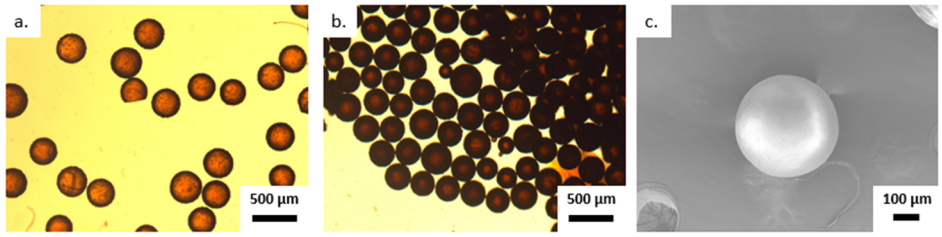

Figure 4. OM images of (a) gel and (b) aerogel microparticles and (c) SEM image of an aerogel microparticle.

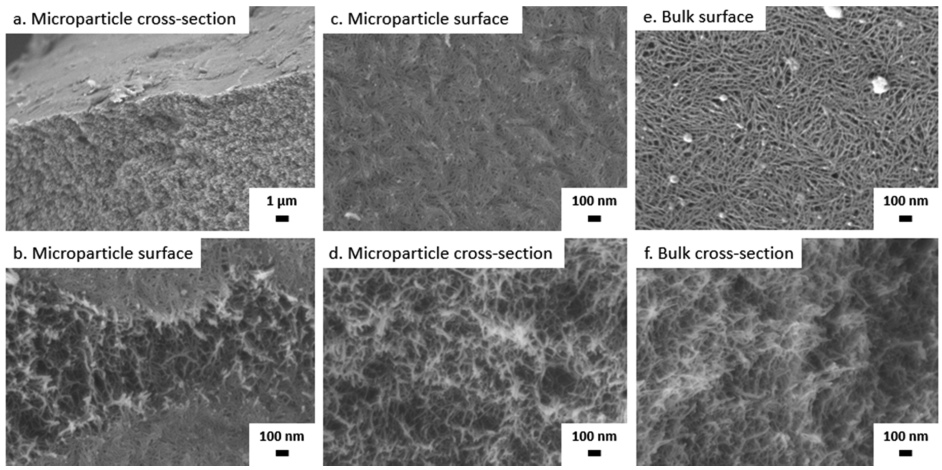

Figure 5. SEM images showing (a) skin layer and internal structure of a microparticle through sectioning, (b) porous internal structure of a microparticle through a tear in the skin layer, (c) skin layer on the surface of a microparticle, (d) cross section of a microparticle, (e) skin layer of the monolith, and (f) cross section of the monolith.

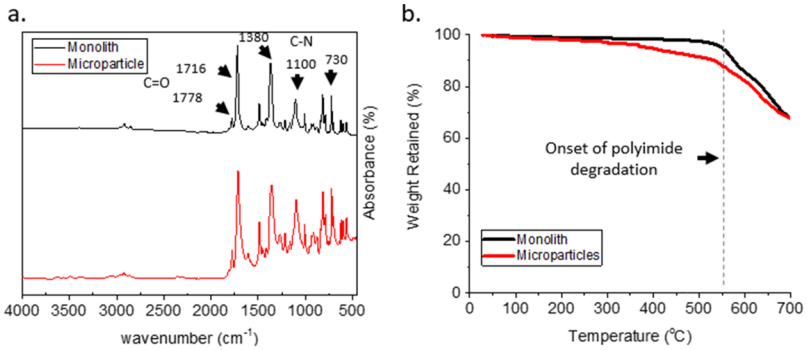

Figure 6. (a) IR spectra and (b) TGA traces of polyimide aerogel monoliths and microparticles.

(Figure 5e) compared to the microparticles (Figure 5c). Note that the gel time was about 26 min for the monoliths, whereas it was estimated to be 10 s for the microparticles, as discussed earlier. The longer gel time in the case of monoliths also allowed much longer time for coarsening of the polymer domains during the liquid–liquid demixing process.[41]

The IR and TGA data presented in Figure 6 present evidence that both the monolith and microparticles had similar chemical properties. Figure 6a shows IR spectra with the peaks at 730, 1100, 1380, 1716, and 1778 cm^{-1}, confirming the presence of the imide functional group. The 1716 and 1778 cm^{-1} absorbance bands correspond to the symmetrical and asymmetrical stretching of the C═O group, respectively, whereas the absorbance band at 730 cm^{-1} is due to the C═O bending. The absorbance bands at 1380 cm^{-1} correspond to C–N stretching in the imide rings, whereas the absorbance band at 1100 cm^{-1} is due to the imide ring deformation. The absence of significant peaks at 1620 and 3000 cm^{-1} indicates that the majority of polyamic acid groups was imidized in the final aerogel materials. The TGA data in Figure 6b show that both monolith and microparticles exhibited good thermal stability at high temperatures. The monolith showed degradation curves typical of polyimides, with a weight loss of 3.5 wt % at 525 °C. The microparticles, however, showed an earlier onset of degradation, with a weight loss of 9.5 wt % at 525 °C. This 6% higher weight loss at 525 °C observed in the case of microparticles can be attributed to residual polyamic acid in the structures that was not fully imidized. We infer that TGA traces show higher sensitivity than IR spectroscopy at detecting low levels of the polyamic acid functional groups in the microparticles. However, at 700 °C, both materials exhibited close values of char yield, for example, 67.7 wt % for monolith and 67.6 wt % for microparticles. The TGA traces

DOI: 10.1021/acs.langmuir.8b03841
Langmuir 2019, 35, 2303–2312

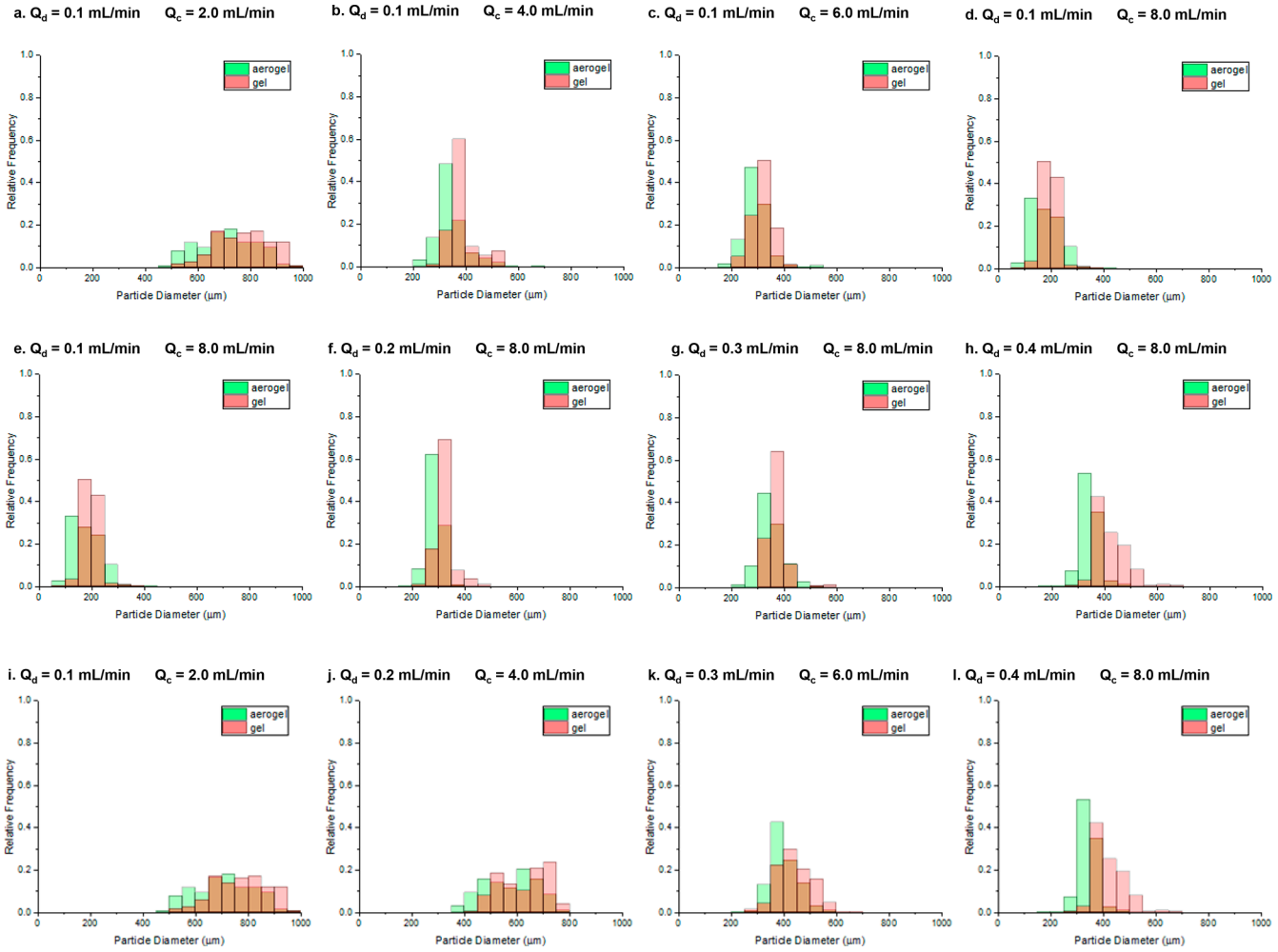

Figure 7. Gel and aerogel microparticle size distributions. The dispersed phase (Q_d) and continuous phase (Q_c) flow rates are indicated in each chart. Red bars correspond to gel microparticles, whereas green bars correspond to aerogel microparticles.

Table 1. Average Gel and Aerogel Microparticle Diameter and Their Associated Shrinkage at Different Flow Conditions

dispersed phase		continuous phase				
flowrate (mL/min)	velocity (m/s)	flowrate (mL/min)	velocity (m/s)	average gel microparticle diameter (μm)	average aerogel microparticle diameter (μm)	shrinkage (%)
0.1	0.048	2	0.018	778 ± 106	713 ± 108	8.4
0.1	0.048	4	0.036	387 ± 50	345 ± 61	10.9
0.1	0.048	6	0.054	319 ± 37	293 ± 50	8.2
0.1	0.048	8	0.072	197 ± 27	182 ± 44	7.6
0.2	0.096	8	0.072	323 ± 33	287 ± 24	11.1
0.3	0.145	8	0.072	374 ± 37	350 ± 49	6.4
0.4	0.193	8	0.072	383 ± 41	342 ± 34	10.7
0.2	0.096	4	0.036	627 ± 88	572 ± 96	8.7
0.3	0.145	6	0.054	441 ± 67	401 ± 51	9.1

presented in Figure 6b are characteristic of polyimide aerogels as reported in the literature.[42]

Microparticle Size Distribution. The microparticle size distribution was studied as functions of the dispersed and continuous phase flow rates. The flow rates were varied following three protocols: (1) continuous phase flow rate (Q_c) was varied for a fixed dispersed phase flow rate (Q_d), (2) Q_d was varied for a given Q_c, and (3) Q_c and Q_d were varied while keeping Q_d/Q_c ratio constant. The data presented in Figure 7 and Table 1 show the effects of various flow conditions on resultant gel and corresponding aerogel microparticle size distributions. The mean volume of an ensemble of aerogel microparticles shows 6−11% shrinkage in reference to the ensemble average volume of the corresponding gel microparticles. These values compare well with the shrinkage data of polyimide aerogel monoliths, ∼10.8% as discussed earlier.

It is apparent from Figure 7 and the data presented in Table 1 that microparticles fabricated exhibited polydispersity in microparticle diameters. This is consistent with the jetting regime of droplet generation.[40] In the jetting regime, a jet of dispersed phase extends from the outlet of the droplet generator and breaks up due to Rayleigh instabilities at a

DOI: 10.1021/acs.langmuir.8b03841
Langmuir 2019, 35, 2303−2312

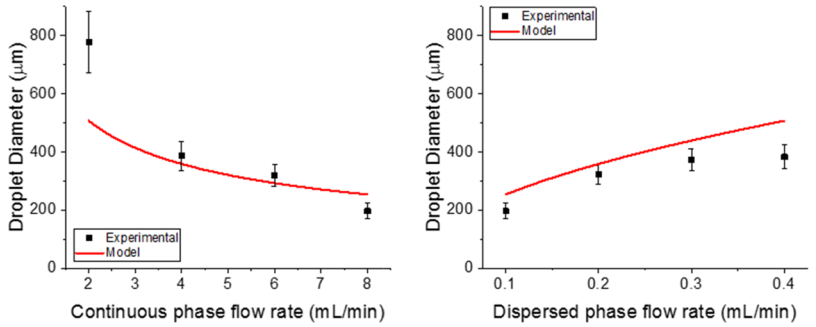

Figure 8. Comparison of experimental droplet size with model prediction of eq 6. (a) Continuous phase flow rate 2−8 mL/min and dispersed phase flowrate 0.1 mL/min. (b) Dispersed phase flowrate 0.1−0.4 mL/min and continuous phase flowrate 8 mL/min.

distance away from the outlet. Jetting was observed in the setup used in the present work because of high viscosity (48.6 mPa s) of the silicone oil acting as the continuous phase compared to a viscosity of 1.98 mPa s of the sol and the low interfacial tension of 3.0 mN/m between the two phases. The polydispersity in microparticle size arises from capillary perturbations of the extended jet, leading to uneven droplet formation.[40] In addition, the average microparticle size is often larger than the diameter of the needle (200 μm). This is indicative of the widening-jet regime,[40] where the dispersed phase velocity is larger than the continuous phase velocity, leading to deceleration of the dispersed phase jet as it extends out into the continuous phase. This results in local buildup of the dispersed phase fluid in the thread undergoing breakup, resulting in uneven droplet sizes.

An exception to the above observation was microparticles fabricated with a dispersed phase flow rate of 0.1 mL/min and the continuous phase flow rate of 8.0 mL/min. This case exhibited an average particle diameter of 197 μm, very close to the diameter of the needle (200 μm) used to deliver the dispersed phase. At these flow conditions, the continuous phase velocity (0.072 m/s) was found to be greater than the dispersed phase velocity (0.048 m/s), indicating that this flow condition had transitioned into the narrowing-jet regime. This set of flow conditions in the narrowing-jet regime also shows the smallest particle size distribution, as a narrowing jet (thinner jet) would suppress the capillary instability, thus producing more monodisperse droplets.[43]

The data presented in Figure 7a−d indicate that an increase of the continuous phase flowrate from 2 to 8 mL/min for a given dispersed phase flow rate of 0.1 mL/min helped reduce the average droplet size from 778 to 197 μm and also produced narrower microparticle size distribution, as reflected in the reduction of standard deviation values from 106 to 27 μm. The reduction of microparticle size can be attributed to an increase of the viscous stress with an increase of the continuous phase flow rate. Note that the interfacial force remained constant in all of these experiments as no surfactant was added. Also, the temperature was not varied during the droplet generation process. The reduction in microparticle size was predicted by Zhu and Wang,[40] expounding on earlier work by Cubaud and Mason[44] as presented in eq 6

$$\frac{D}{w_o} = g(k^*)(\varphi)^{0.5} \tag{6}$$

In eq 6, D is the droplet diameter, w_o is the width of the outer channel, $g(k^*)$ is a function of the wavenumber k^* with $g(k^*) \approx 1.43$, and φ is the ratio of the dispersed and continuous phase flow rates, Q_d/Q_c. A comparison of the experimental and predicted droplet size based on eq 6 is shown in Figure 8a.

The relationship in eq 6 developed for the narrow-jetting regime also shows good correlation with the experimental droplet diameter data, particularly for higher continuous phase flow rates if the continuous phase velocity was higher or similar to the dispersed phase velocity. However, at a low continuous phase flow rate of 2 mL/min, a significant deviation of the experimental droplet size occurred from the prediction of eq 6. The continuous phase velocity of 0.07 m/s and the dispersed phase velocity of 0.19 m/s in this case belong to the widening-jet regime, where eq 6 is no longer valid. This aspect, however, will be considered in a future study.

The effects of dispersed phase flowrate are now analyzed. It is apparent from the data presented in Figure 7e−h that an increase of the dispersed phase flow rate from 0.1 to 0.4 mL/min also produced an increase of the average diameter of gel microparticles from 197 ± 27 to 383 ± 41 μm. The experimentally obtained mean droplet diameter values were also compared to the prediction of eq 6, as presented in Figure 8b. A good correlation is found for continuous phase velocity higher or equal to the dispersed phase velocity, for example, when the dispersed phase flow rate was less than 0.3 mL/min. At higher dispersed phase flow rates such as 0.4 mL/min, the system once again transitioned to a widening-jet regime, resulting in a deviation from the prediction of eq 6.

Finally, the effects of an increase of both the dispersed and continuous phase flow rates were investigated by varying the values of Q_c and Q_d while keeping the ratio Q_d/Q_c constant, for example, Q_c = 0.1 mL/min; Q_d = 2 mL/min to Q_c = 0.4 mL/min; Q_d = 8 mL/min. The data presented in Figure 7i−l and Table 1 show that the gel microparticle size reduced from 778 ± 106 to 383 ± 41 μm with an increase of the flow rates in the dispersed and continuous phases. It is apparent from such data that the higher the continuous phase flow rate for a given ratio Q_d/Q_c, the smaller the average gel microparticle diameter and the narrower the distribution of gel microparticle size. For the above flow conditions, the dispersed phase velocity was 2.67 times the continuous phase velocity, leading to significant deviations from the predicted droplet size as in eq 6. In view of this, a comparison with the narrowing-jet regime model was not attempted.

Effect of Temperature. Recall that silicone oil in the oil bath was heated to expedite cross-linking and gelation of the sol droplets. At this point, it is unknown if the temperature of the oil bath exerted an effect on the microparticle morphology. In view of this, the silicone oil bath temperature was varied in

DOI: 10.1021/acs.langmuir.8b03841
Langmuir 2019, 35, 2303−2312

the range 60−100 °C. The morphology of the aerogel microparticles produced with dispersed and continuous phase flow rates of, respectively, 0.3 and 6 mL/min was analyzed. The gel and aerogel microparticle size distributions are presented in Figure S2. Table 2 lists the average size of gel and aerogel microparticles along with data on diameter shrinkage and BET surface area. It is evident that gel microparticle diameter reduced from 563 ± 140 to 395 ± 44 μm with an increase of the temperature of the oil bath from 60 to 100 °C. The OM images in the insets of Figure S2 present visual impression that with an increase of the oil bath temperature, the gel microparticles experienced higher shrinkage and correspondingly higher density, the latter inferred from an increase of the opacity of the microparticles.

Table 2. Average Gel and Aerogel Diameter, Shrinkage, and BET Surface Area of Aerogel Microparticles as a Function of Silicone Oil Bath Temperatures[a]

temperature (°C)	average gel microparticle diameter (μm)	average aerogel microparticle diameter (μm)	diameter shrinkage (%)	BET surface area (m^2/g)
60	563 ± 140	546 ± 129	3.0	484
70	516 ± 109	494 ± 102	4.3	431
80	492 ± 93	452 ± 68	8.1	412
90	441 ± 67	405 ± 56	8.2	409
100	395 ± 44	376 ± 52	4.8	369

[a]Dispersed and continuous phase flow rates were, respectively, 0.3 and 6 mL/min.

The hysteresis loops seen in BET isotherms in Figure 9 indicate significant mesoporosity (pore diameter 2−50 nm) in aerogel microparticles. The surface area data listed in Table 2 indicate that the aerogel microparticles had high surface area, 360−484 m^2/g. The surface area of corresponding monolithic aerogels was higher, 537 m^2/g. The relatively lower BET surface area in the case of aerogel microparticles is due to significant fraction of skin layers that formed on the particle surfaces. Note that aerogel microparticles reported in Table 2 had significantly higher surface area to volume ratio (11−15 1/mm) than the monoliths (0.4 1/mm). The surface area to volume ratio of cylindrical aerogel monoliths was calculated based on the actual diameter of 11.6 mm and length of 22.6 mm.

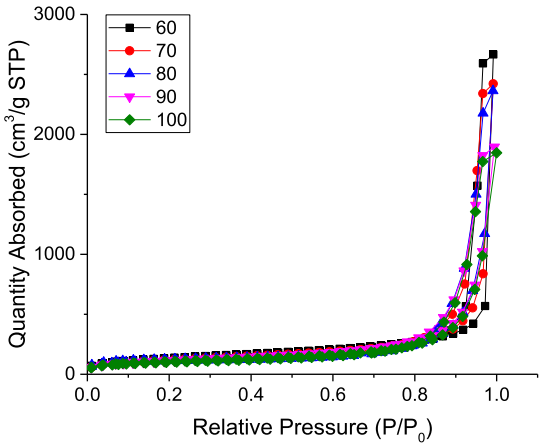

Figure 9. BET isotherms for aerogel microparticles fabricated with varying silicone oil bath temperature.

The BET surface area reported in Table 2 reduced with an increase of bath temperature, for example, 484 m^2/g at 60 °C to 369 m^2/g at 100 °C. This is commensurate with a reduction of area under the hysteresis loops formed by the adsorption and desorption isotherms in the BET curves (Figure 9) indicating reduction of mesopore fractions.

We now examine the morphology of the surfaces of aerogel microparticles. Figure 10a shows that the microparticles fabricated at 60 °C exhibit porous skin layer morphology similar to what was observed for monolithic aerogels, for example, in Figure 5e. Figure 10a also shows that the skin layer of the microparticles was composed of fibrillar strands of 10−20 nm diameter. The particle surface remained porous and retained fibrillar morphology as the temperature of the silicone oil bath was increased; however, the skin layers developed wrinkles. The degree of wrinkling increased with an increase of the temperature from 70 to 90 °C, as shown in Figure 10b−d. Such wrinkles can be attributed to outward flow of DMF from inside the droplets caused by higher solubility of DMF in silicone oil at higher temperature. This also caused a reduction of the volume of gel particles, measured from reduction of particle diameter as presented in Table 2. However, at 100 °C, the fibrous morphology of the particle surface was lost (Figure 10e), as the miscibility of DMF with silicone oil reached a point where the outflow of DMF was so high that the polyimide precipitated out of the solution within a thin shell near the surface. This is also reflected in OM images in Figure S2, where the microparticles appeared dense and dark compared to the translucent microparticles obtained at other temperatures.

We anticipated that the use of high silicone oil bath temperature would also increase the rate of polyamic acid formation and expedite imidization reactions, thus promoting faster gel formation. In view of the aerogel microparticle morphology discussed above in conjunction with Figure 10, we now accept that higher silicone oil temperature also increased the solubility between DMF and silicone oil. In this context, one can describe the fate of a polyimide sol droplet as it enters hot silicone oil. First, it experiences a temperature spike in a thin shell within the droplets. Second, the shell gels almost

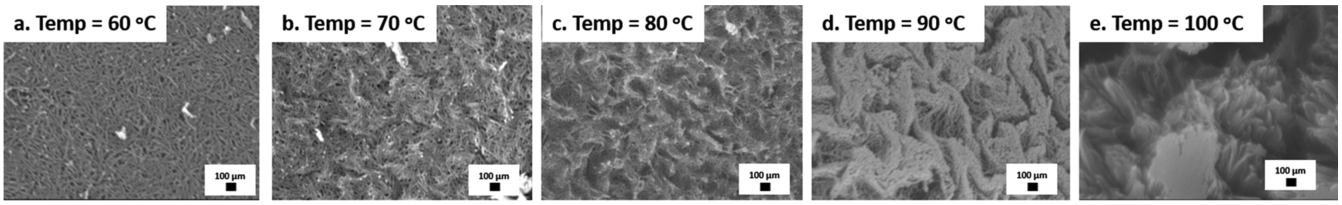

Figure 10. Skin layer of aerogel microparticles synthesized at various silicone oil bath temperatures of (a) 60, (b) 70, (c) 80, (d) 90, and (e) 100 °C.

DOI: 10.1021/acs.langmuir.8b03841
Langmuir 2019, 35, 2303−2312

Table 3. Shrinkage, Porosity, and Pore Size Distribution of Monolithic Aerogels Cured at Various Temperatures

temperature (°C)	diameter (mm)	shrinkage (%)	porosity (%)	micropore percent	mesopore percent	macropore percent
20	11.2 ± 0.0	13.9 ± 0.0	97.0 ± 0.0	0.5	2.1	97.4
40	11.3 ± 0.0	13.3 ± 0.2	97.2 ± 0.0	0.7	2.7	96.6
60	11.5 ± 0.2	12.4 ± 0.2	97.6 ± 0.0	0.6	2.4	97.0
80	11.7 ± 0.1	10.4 ± 0.3	98.0 ± 0.0	0.5	2.0	97.5
100	11.7 ± 0.1	10.0 ± 0.3	97.6 ± 0.0	0.5	2.9	96.6

immediately (<10 s) thus forming a solid porous skin around the droplet. Third, almost simultaneously, higher solubility of DMF in silicone oil results in a net fluid flow out of the liquid droplets into the continuous phase, thus resulting in shrinkage and wrinkling of the already formed shell. The increase in solubility of DMF in silicone oil with an increase of temperature was inferred qualitatively in a separate experiment as presented Figure S3 in the Supporting Information.

In view of the strong temperature effects on aerogel microparticle morphology, a separate set of experiments were conducted on a polyimide gel monolith to determine if higher imidization temperature also had any effect on skin morphology, bulk morphology, and porosity of the monolithic aerogels. For this purpose, monolithic polyimide gels were cured in an oven at 20, 40, 60, 80, and 100 °C followed by supercritical drying to obtain corresponding aerogel specimens. Table 3 shows the effect of temperature on properties of monolithic polyimide aerogels.

It is seen that an increase of imidization temperature led to a reduction of shrinkage of the aerogels. For monoliths synthesized at 60 °C, the average diameter of the final aerogels was 11.5 mm, whereas monoliths synthesized at 100 °C had an average diameter of 11.7 mm. Comparing these two monoliths, a 1.7% increase in aerogel diameter is observed as the curing temperature was increased from 60 to 100 °C. Under the same thermal treatment, as discussed earlier, the aerogel microparticles experienced a 30% reduction in average microparticle diameter from 563 to 395 μm as the silicone oil bath temperature was increased from 60 to 100 °C. The data in Table 3 also show that calculated porosities of the monoliths are within a narrow range of 97.0−98.0%. The pore size distribution also shows that the monoliths cured at various temperature are predominantly macroporous, with macropore fraction in the range of 96.6−97.5%, indicating that the internal strand structure did not change significantly at higher temperature. The data presented in Table 3 confirm that wrinkling of aerogel microparticle skin layer was caused by shrinkage of the outer layer of microparticles due to out flow of DMF into silicone oil promoted by higher solubility.

CONCLUSIONS

The results presented in this paper establish that polyimide gel and aerogel microparticles can be successfully synthesized using a coflow microfluidic setup from surfactant-free oil-in-oil systems. The rapid sol to gel transition is achieved using a hot silicone oil bath decoupled from the droplet generation system, thus avoiding coalescence of sol droplets and expediting transformation of sol droplets into discrete gel droplets of the spherical structure. The use of a microfluidic droplet generator enables the control of microparticle size through both the dispersed and continuous phase flowrates, resulting in the synthesis of aerogel microparticles with an average diameter of 197 μm and narrow microparticle size distribution. The results also show significant wrinkling of the aerogel microparticle surfaces attributed to out flow of DMF into hot silicone oil and shrinkage of the thin shell near the microparticle surfaces.

ASSOCIATED CONTENT

Supporting Information

The Supporting Information is available free of charge on the ACS Publications website at DOI: 10.1021/acs.langmuir.8b03841.

Additional data on jetting regime and the effects of temperature on microparticle size and oil−oil phase solubility (PDF)

AUTHOR INFORMATION

Corresponding Author

*E-mail: janas@uakron.edu.

ORCID

Sadhan C. Jana: 0000-0001-8962-380X

Notes

The authors declare no competing financial interest.

ACKNOWLEDGMENTS

This work is partially funded by National Science Foundation under grant number CMMI 1826030.

REFERENCES

(1) Kim, S. J.; Chase, G.; Jana, S. C. The Role of Mesopores in Achieving High Efficiency Airborne Nanoparticle Filtratrion Using Aerogel Monoliths. *Sep. Purif. Technol.* **2016**, *166*, 48−54.

(2) Gu, S.; Zhai, C.; Jana, S. C. Aerogel Microparticles from Oil-in-Oil Emulsion Systems. *Langmuir* **2016**, *32*, 5637−5645.

(3) Meador, M. A. B.; Malow, E. J.; Silva, R.; Wright, S.; Quade, D.; Vivod, S. L.; Guo, H.; Guo, J.; Cakmak, M. Mechanically Strong, Flexible Polyimide Aerogels Cross-Linked with Aromatic Triamine. *ACS Appl. Mater. Interfaces* **2012**, *4*, 536−544.

(4) Kistler, S. S. Coherent Expanded Aerogel Jellies. *Nature* **1931**, *127*, 741.

(5) Kim, S. J.; Chase, G.; Jana, S. C. Polymer Aerogels for Efficient Removal of Airborne Nanoparticles. *Sep. Purif. Technol.* **2015**, *156*, 803−808.

(6) Daniel, C.; Alfano, D.; Venditto, V.; Cardea, S.; Reverchon, E.; Larobina, D.; Mensitieri, G.; Guerra, G. Aerogels with a Microporous Crystalline Host Phase. *Adv. Mater.* **2005**, *17*, 1515−1518.

(7) Lee, J. K.; Gould, G. L.; Rhine, W. Polyurea based aerogel for a high performance thermal insulation material. *J. Sol-Gel Sci. Technol.* **2008**, *49*, 209−220.

(8) Leventis, N.; Chidambareswarapattar, C.; Bang, A.; Sotiriou-Leventis, C. Cocoon-in-Web-Like Superhydrophobic Aerogels from Hydrophilic Polyurea and Use in Environmental Remediation. *ACS Appl. Mater. Interfaces* **2014**, *6*, 6872−6882.

(9) Shinko, A.; Jana, S. C.; Meador, M. A. Crosslinked Polyurea Aerogels with Controlled Porosity. *RSC Adv.* **2015**, *5*, 105329−105338.

(10) Guo, H.; Meador, M. A. B.; McCorkle, L.; Quade, D. J.; Guo, J.; Hamilton, B.; Cakmak, M.; Sprowl, G. Polyimide Aerogels Cross-

DOI: 10.1021/acs.langmuir.8b03841
Langmuir 2019, 35, 2303−2312

Linked through Amine Functionalized Polyoligomeric Silsesquioxane. *ACS Appl. Mater. Interfaces* **2011**, *3*, 546−552.
(11) Leventis, N.; Sotiriou-Leventis, C.; Mohite, D. P.; Larimore, Z. J.; Mang, J. T.; Churu, G.; Lu, H. Polyimide Aerogels by Ring-Opening Metathesis Polymerization (ROMP). *Chem. Mater.* **2011**, *23*, 2250−2261.
(12) Zhai, C.; Jana, S. C. Tuning Porous Networks in Polyimide Aerogels for Airborne Nanoparticle Filtration. *ACS Appl. Mater. Interfaces* **2017**, *9*, 30074−30082.
(13) Wang, X.; Jana, S. C. Tailoring of Morphology and Surface Properties of Syndiotactic Polystyrene Aerogels. *Langmuir* **2013**, *29*, 5589−5598.
(14) Gu, S.; Jana, S. C. Open Cell Aerogel Foams with Hierarchical Pore Structures. *Polymer* **2017**, *125*, 1−9.
(15) Teo, N.; Jana, S. C. Open Cell Aerogel Foams via Emulsion Templating. *Langmuir* **2017**, *33*, 12729−12738.
(16) Teo, N.; Gu, Z.; Jana, S. C. Polyimide-Based Aerogel Foams Via Emulsion-Templating. *Polymer* **2018**, *157*, 95−102.
(17) García-González, C. A.; Alnaief, M.; Smirnova, I. Polysaccharide-Based Aerogels—Promising Biodegradable Carriers for Drug Delivery Systems. *Carbohydr. Polym.* **2011**, *86*, 1425−1438.
(18) Quignard, F.; Valentin, R.; Di Renzo, F. Aerogel Materials from Marine Polysaccharides. *New J. Chem.* **2008**, *32*, 1300−1310.
(19) Alnaief, M.; Alzaitoun, M. A.; García-González, C. A.; Smirnova, I. Preparation of Biodegradable Nanoporous Microspherical Aerogel Based on Alginate. *Carbohydr. Polym.* **2011**, *84*, 1011−1018.
(20) Grace, H. P. Dispersion Phenomena in High Viscosity Immiscible Fluid Systems and Application of Static Mixers as Dispersion Devices in Such Systems. *Chem. Eng. Commun.* **1982**, *14*, 225−277.
(21) Alnaief, M.; Smirnova, I. In Situ Production of Spherical Aerogel Microparticles. *J. Supercrit. Fluids* **2011**, *55*, 1118−1123.
(22) Kwon, J.; Kim, J.; Yoo, T.; Park, D.; Han, H. Preparation and Characterization of Spherical Polyimide Aerogel Microparticles. *Macromol. Mater. Eng.* **2014**, *299*, 1081−1088.
(23) Moner-Girona, M.; Roig, A.; Molins, E.; Llibre, J. Sol-Gel Route to Direct Formation of Silica Aerogel Microparticles Using Supercritical Solvents. *J. Sol-Gel Sci. Technol.* **2003**, *26*, 645−649.
(24) Zhang, Y.; Wang, J.; Zhang, X. Surfactant-Free Synthesis of Silica Aerogel Microspheres with Hierarchically Porous Structure. *J. Colloid Interface Sci.* **2018**, *515*, 1−9.
(25) Cramer, C.; Fischer, P.; Windhab, E. J. Drop Formation in a Co-Flowing Ambient Fluid. *Chem. Eng. Sci.* **2004**, *59*, 3045−3058.
(26) Utada, A. S.; Fernandez-Nieves, A.; Stone, H. A.; Weitz, D. A. Dripping to Jetting Transitions in Coflowing Liquid Streams. *Phys. Rev. Lett.* **2007**, *99*, 094502.
(27) Zhu, P.; Kong, T.; Kang, Z.; Tian, X.; Wang, L. Tip-Multi-Breaking in Capillary Microfluidic Devices. *Sci. Rep.* **2015**, *5*, 11102.
(28) Christopher, G. F.; Anna, S. L. Microfluidic Methods for Generating Continuous Droplet Streams. *J. Phys. D: Appl. Phys.* **2007**, *40*, R319.
(29) Vladisavljević, G. T.; Khalid, N.; Neves, M. A.; Kuroiwa, T.; Nakajima, M.; Uemura, K.; Ichikawa, S.; Kobayashi, I. Industrial Lab-on-a-Chip: Design, Applications and Scale-up for Drug Discovery and Delivery. *Adv. Drug Delivery Rev.* **2013**, *65*, 1626−1663.
(30) Lian, M.; Patrick Collier, C.; Doktycz, M. J.; Retterer, S. T. Monodisperse Alginate Microgel Formation in a Three-Dimensional Microfluidic Droplet Generator. *Biomicrofluidics* **2012**, *6*, 044108.
(31) Yeh, C.-H.; Chen, Y.-C.; Lin, Y.-C. Generation of Droplets with Different Concentrations Using Gradient-Microfluidic Droplet Generator. *Microfluid. Nanofluid.* **2011**, *11*, 245−253.
(32) Xu, Q.; Nakajima, M. The Generation of Highly Monodisperse Droplets through the Breakup of Hydrodynamically Focused Microthread in a Microfluidic Device. *Appl. Phys. Lett.* **2004**, *85*, 3726−3728.
(33) Dendukuri, D.; Tsoi, K.; Alan Hatton, T.; Doyle, P. S. Controlled Synthesis of Nonspherical Microparticles Using Microfluidics. *Langmuir* **2005**, *21*, 2113−2116.
(34) Umbanhowar, P. B.; Prasad, V.; Weitz, D. A. Monodisperse Emulsion Generation via Drop Break Off in a Coflowing Stream. *Langmuir* **2000**, *16*, 347−351.
(35) Zhang, J. M.; Li, E. Q.; Thoroddsen, S. T. A Co-Flow-Focusing Monodisperse Microbubble Generator. *J. Micromech. Microeng.* **2014**, *24*, 035008.
(36) Quell, A.; Elsing, J.; Drenckhan, W.; Stubenrauch, C. Monodisperse Polystyrene Foams via Microfluidics − A Novel Templating Route. *Adv. Eng. Mater.* **2015**, *17*, 604−609.
(37) Crespy, D.; Landfester, K. Making Dry Fertile: A Practical Tour of Non-Aqueous Emulsions and Miniemulsions, Their Preparation and Some Applications. *Soft Matter* **2011**, *7*, 11054−11064.
(38) Marqusee, J. A.; Ross, J. Kinetics of Phase Transitions: Theory of Ostwald Ripening. *J. Chem. Phys.* **1983**, *79*, 373−378.
(39) Li, T.; Zhao, L.; Liu, W.; Xu, J.; Wang, J. Simple and Reusable Off-the-Shelf Microfluidic Devices for the Versatile Generation of Droplets. *Lab Chip* **2016**, *16*, 4718−4724.
(40) Zhu, P.; Wang, L. Passive and Active Droplet Generation with Microfluidics: A Review. *Lab Chip* **2017**, *17*, 34−75.
(41) Teo, N.; Jana, S. C. Solvent Effects on Tuning Pore Structures in Polyimide Aerogels. *Langmuir* **2018**, *34*, 8581−8590.
(42) Chidambareswarapattar, C.; Larimore, Z.; Sotiriou-Leventis, C.; Mang, J. T.; Leventis, N. One-Step Room-Temperature Synthesis of Fibrous Polyimide Aerogels from Anhydrides and Isocyanates and Conversion to Isomorphic Carbons. *J. Mater. Chem.* **2010**, *20*, 9666−9678.
(43) Anna, S. L. Droplets and Bubbles in Microfluidic Devices. *Annu. Rev. Fluid. Mech.* **2016**, *48*, 285−309.
(44) Cubaud, T.; Mason, T. G. Capillary Threads and Viscous Droplets in Square Microchannels. *Phys. Fluids* **2008**, *20*, 053302.

DOI: 10.1021/acs.langmuir.8b03841
Langmuir 2019, 35, 2303−2312